Solid State Communications 363 (2023) 115103

Contents lists available at ScienceDirect

Solid State Communications

journal homepage: www.elsevier.com/locate/ssc

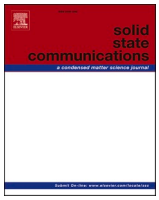

Properties of the double half-heusler alloy $ScNbNi_2Sn_2$ with respect to structural, electronic, optical, and thermoelectric aspects

H. Mekki [a,b], H. Baaziz [a,b,*], Z. Charifi [a,b], T. Ghellab [a,b], A.E. Genç [c], Ş. Uğur [c], G. Uğur [c]

[a] Department of Physics, Faculty of Science, University of M'sila, 28000, M'sila, Algeria
[b] Laboratory of Physics and Chemistry of Materials, University of M'sila, Algeria
[c] Department of Physics, Faculty of Science, Gazi University, 06500, Ankara, Turkey

ARTICLE INFO

Communicated by L. Brey

Keywords:
Double half-heusler
Optoelectronic
Thermoelectric properties

ABSTRACT

In the current work, the structural, electronic, thermoelectrics, and optical characteristics of the double half Heusler (DHH) $ScNbNi_2Sn_2$ compound are reported for the first time using density functional theory (DFT). The computed band structures show typical semiconductor behavior with an indirect bandgap (0.47 eV) using EV-GGA approximation. We also investigated the optical properties such as the dielectric function, optical conductivity, refractive index. Boltzmann's semiclassical theory attempts to explain a simulation concept in the BoltzTrap software, and the findings were presented and analyzed in terms of electrical conductivity, electronic and lattice thermal conductivities, the Seebeck coefficient, and the Figure of merit over a 50 K–1000 K temperature range. At room temperature, with a low magnitude of lattice thermal conductivity (κ_L) (5.30776 W/m.K) and a maximum value of the merit factor (ZT) is 0.64 at 900 K for $ScNbNi_2Sn_2$ compound is observed. These findings suggest that our material may be a viable option for use in high-temperature thermoelectric devices. We calculated (S, (σ/τ), (k_e/τ)) along the x, y, and z axes utilizing the EV-GGA method. We found out that our compound is thermoelectrically anisotropic. We have also studied in EV-GGA the effect of the carrier concentration on the Seebeck coefficnet at T = 600 K. The maximum value of S is 356.9905 μV/K with $n = 3.04 \times 10^{19} Cm^{-3}$ within GGA and EV-GGA respectively.

1. Introduction

In the last decade, studies into the thermoelectric characteristics of half-Heusler compounds have garnered a lot of interest [1–3]. Multiple examples of advanced thermoelectric materials (YFeSb (Y=Nb, Ta) [4,5], and ZrCoBi [6] are *p*-type transport materials, while TiNiSn [7,8] is *n*-type) included in this group of compounds due to the wide chemical space available to tailor their characteristics. The remarkable electrical transport capabilities of half-Heusler compounds are largely responsible for their outstanding performance [9]. Ternary half-Heusler materials, however, have a disadvantage when compared to the top IV-VI compounds based thermoelectric materials [10,11] owing to their inherently high lattice thermal conductivity (k_L). When compared to other high-performance materials with a half-Heusler formula (T = 300 K), ZrCoBi [6] has a k_L of just 10 W/(m.K), where today's leading thermoelectric material PbTe has an intrinsic k_L of just 2 W/(m.K) [12]. Because of this, it is better to devise a method for locating novel semiconductors that exhibit the electronic characteristics of half-Heusler alloys but have substantially lower k_L.

Although k_L is known to be compositionally dependent via phonon scattering [13,14] and Mechanisms for softening the lattice [6,14], it is also known to be dependent on the size of the primitive unit cell [15]. The value of k_L relies mostly on N which represent the total number of atoms in the elementary unit cell, even for solids with comparable bulk characteristics including Debye temperature, average cell mass, particular thermal capacity, and Gruneisen values [15]. Lower k_L in complex materials with higher N is caused by a lesser percentage of high group velocity (v_g) acoustic modes opposed to smaller (v_g) optical modes. The materials $La_2Mo_2O_9$ ($N = 624$, $k_L = 0.7$ W m^{-1} K^{-1} [16] and $Yb_{14}AlSb_{11}$ ($N = 104$, $k_L = 0.6$ W m^{-1} K^{-1}) [15,17] are two illustrious instances of high N compounds with low k_L values. Nonetheless, N = 3 for ternary half-Heuslers, revealing a vast untapped resource for the discovery of materials with low thermal conductivity if the effective N might be consistently increased. The perovskite type is the basis for a famous group of materials with a wide range of cell sizes [18]. Ternary perovskites ABO_3 (eg, $BaTiO_3$) have $N = 5$, whereas quaternary double

* Corresponding author. Department of Physics, Faculty of Science, University of M'sila, 28000, M'sila, Algeria.
E-mail addresses: baaziz_hakim@yahoo.fr, hakim.baaziz@univ-msila.dz (H. Baaziz).

https://doi.org/10.1016/j.ssc.2023.115103
Received 25 December 2022; Received in revised form 12 February 2023; Accepted 13 February 2023
Available online 17 February 2023

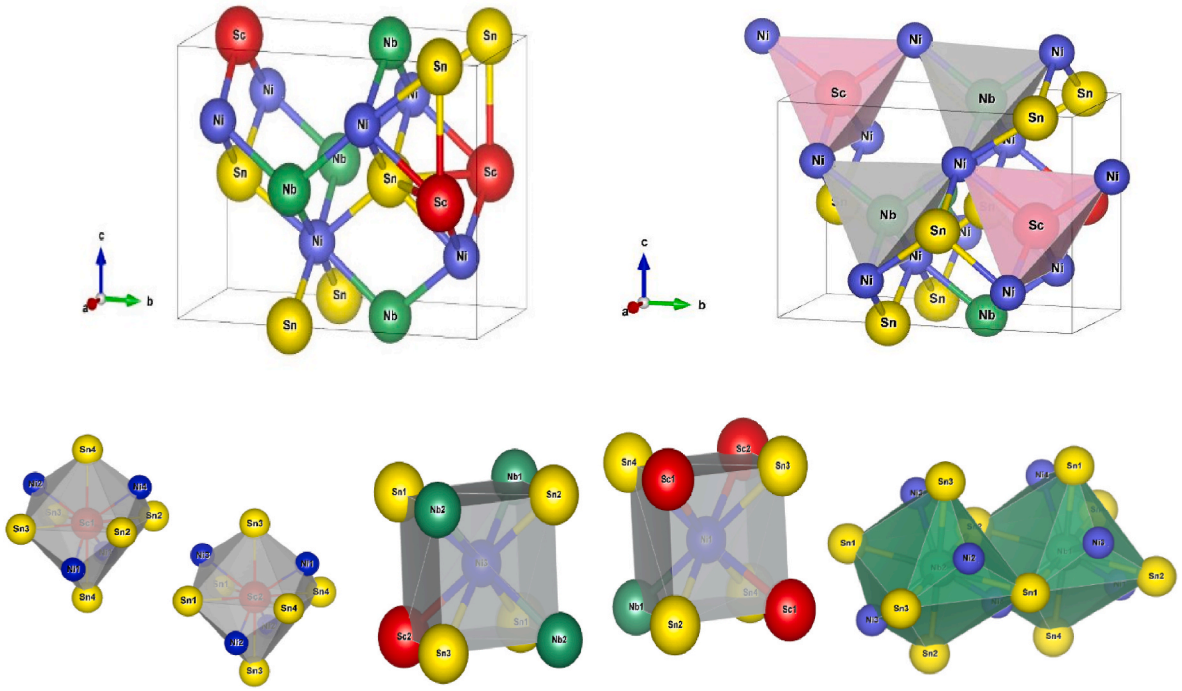

Fig. 1. Crystal structure of the double half-Heusler $ScNbNi_2Sn_2$ compound. The red, green, blue, and yellow spheres represent the Sc, Nb, Ni, and Sn atom. (For interpretation of the references to colour in this figure legend, the reader is referred to the Web version of this article.)

perovskites ($A_2B'B''O_6$, for instance, Sr_2FeMoO_6 ($N = 10$), La_2CuSnO_6 ($N = 40$)) possess $N \geq 10$ [19]. When compared to single perovskites, double perovskites provide more flexibility in terms of modifying their functions for photovoltaic devices, magnetoresistive characteristics, etc [18,20–22]. When compared to single perovskite compounds, double perovskites can be found in vastly greater quantities, thanks to the possibilities presented by the introduction of a second element [18,20]. Half-Heuslers can be made from a wide variety of elements, similar to perovskites, with each site possessing a different group from the periodic table. According to the valence balancing rule [23], in the most stable forms, the combined net valence (NV) of the three elements is zero. Therefore, this data can be utilized to select the most appropriate ternary half-Heusler elements (mostly XYZ) to implement. Isovalent substitution between compounds with no distinctive valence balanced combination is typically the focus of studies on the quaternary combinations of the half-Heusler phases (such as $Ti_{0.5}Zr_{0.5}NiSn$ and $Ti_{0.2}Zr_{0.8}NiSn$), which does not encourage the creation of ordered substances such as the double perovskites [24]. Many alloy compositions create disordered solutions that are only maintained at elevated temperatures. Nonetheless, the combination generating 18-electron ternary half-Heuslers [23] is characterized by aliovalent substitution, which may result in a novel combination with balanced valence (Iron and Nickel substitutions on the atomic Y-site of Ti2FeNiSb2 are one example). Accordingly, we anticipate ordered ground states at these one-of-a-kind combinations to form stable complexes, precisely as ternary half-Heuslers [25]. We describe double half-Heuslers ($X_2Y'Y''Z_2$ vs XYZ, with Y′ and Y″ not being isovalent) as the stability of quaternary compounds is contingent upon aliovalent substitution; this definition is inspired by the concept of double perovskites, where the "double" might allude to perovskite formula unit doubling ($A_2B'B''O_6$ vs ABO_3). These aliovalently substituted materials (for instance, $Ti_2FeNiSb_2$) are called double half-Heuslers to set them apart from other quaternary arrangements containing isovalent alloys (e.g., $Ti_{0.5}Zr_{0.5}NiSn$), despite the fact that they may or may not undergo an order-disorder transition at higher temperatures. The double half-Heusler mixture ensures that the effective N for kL is greater than 3, despite the disordered phase having a potentially larger scattering mechanism for phonons. When compared to the ternary compositions, the double half-Heusler structures' quaternary components may offer a much larger spatial structure in which new compounds can be discovered. Very many stable double half-Heuslers have been predicted, but none have yet been found in experiments. For the same reasons that ternary half-Heuslers are being investigated [26], double half-Heuslers may find utility in areas as diverse as thermoelectrics, transparent conductive thin films (e.g., TaIrGe [27]), paradoxical semi-metals (e.g., HfIrAs [25]), and spintronics (e.g., $V_{0.8+\delta}CoSb$ [28,29]).

Our research aims to characterize ScNbNi2Sn2's electronic behavior, including its band structure and density of state (DOS), as well as its thermoelectric capabilities, including its Seebeck coefficient. Boltzmann's semiclassical theory is used to describe a computational model, and the resulting electrical conductivity, electronic thermal conductivity, Seebeck coefficient, and figure of merit are reported. Furthermore, the optical properties (dielectric function, optical conductivity, etc.) are determined. However, no similar research exists in the literature.

2. Specifics of the computation

The computations are carried out using the linearized augmented plane wave [30] as implemented in the Wien2k code [31], which is founded on first-principles density functional theory (DFT) [32]. The exchange-correlation energy is parameterized by the generalized gradient approximation GGA-PBE [33] and the local density approximation LDA [34], and to obtain a more precise electronic structure the modified Beck-Johnson potential [35] and Engel-Vosko approximation (EV-GGA) [36]. Given that the lowest muffin-tin radius (R.M.T) is between 2.28 and 2.42 atomic units (a.u.), and that the largest modulus of reciprocal vector K_{max} occurs in the first *Brillouin zone*, we set the R.M.T $\times$ K_{max} value equal to 9. Within the muffin tin, $l_{max} = 10$ and $G_{max} = 14$ have been entered as the wave function expansion parameters, with G_{max} denoting the magnitude of the biggest vector in the Fourier expansion of the charge density. The inclusion of 1000 k-points in the *Brillouin zone* guarantees the precision of the calculations. The self-consistent calculation is considered to be converged when the total energy difference is 10^{-4} Ry. The Thermoelectric (TE) properties were

Table 1
The atomic positions of the double half Heusler $ScNbNi_2Sn_2$.

Atom	x	y	z
Nb	0.00000000	0.37347500	0.50000000
	0.50000000	0.62652500	0.00000000
Ni1	0.00000000	0.13507300	0.73516800
	0.50000000	0.86492700	0.23516800
Ni2	0.00000000	0.61712200	0.75465800
	0.50000000	0.38287800	0.25465800
Sc	0.50000000	0.12255800	0.98976200
	0.00000000	0.87744200	0.48976200
Sn1	0.50000000	0.62574100	0.50200300
	0.00000000	0.37425900	0.00200300
Sn2	0.00000000	0.87545300	0.98729500
	0.50000000	0.12454700	0.48729500

Table 2
Calculated structural parameters lattice (Å), bulk modulus B (GPa) and its first derivative B′, energy (Ryd), and bond lengths (Å) for $ScNbNi_2Sn_2$ compound using GGA and LDA approximations.

Compound	Physical parameters	Approximation	
		GGA	LDA
$ScNbNi_2Sn_2$	$a(A^0)$	4.2873	4.1912
31_Pmn2₁	*b*	8.6064	8.4133
	c	6.0740	5.9389
	b/a	2.0074	2.0073
	c/a	1.4167	1.4169
	E_{min}(Ryd)	−79939.0489	−79854.1487
	B(GPa)	120.81	146.09
	B`	4.5349	4.8336
	$d_{Sc\text{-}Ni1}$	2.646 (x3)	2.586 (x3)
	$d_{Sc\text{-}Ni2}$	2.758 (x1)	2.697 (x1)
	$d_{Sc\text{-}Sn1}$	3.049 (x3)	2.98 (x3)
	$d_{Sc\text{-}Sn2}$	3.0231 (x3)	2.95 (x3)
	$d_{Nb\text{-}Ni1}$	2.5005 (x1)	2.44 (x1)
	$d_{Nb\text{-}Ni2}$	2.6125 (x3)	2.55 (x3)
	$d_{Nb\text{-}Sn1}$	3.05024 (x3)	2.983 (x3)
	$d_{Nb\text{-}Sn2}$	3.0259 (x3)	2.96 (x3)

calculated using the Boltzmann semi-classical transport equation implemented in the BoltzTraP code [37] under constant relaxation time approximation (τ).

3. Result and analysis

3.1. Structural aspects

This section examines the structural characteristics of our double half-Heusler $ScNbNi_2Sn_2$ alloy. This kind of research is of great importance because it permits the collection of information on microstructure of compounds, it has major implications for the foreseeing of other features including electronic, optical, and thermoelectric ones.

Half-Heusler (HH) compounds semiconductors are considered an ideal candidate for thermoelectric devices which has the chemical formula XYZ. As previously stated, the new class of Heusler compounds is called double half-Heusler and it is a quaternary compound where the words "double" refer to doubling the half-Heusler chemical formula converts to $X_2Y'Y''Z_2$, where Y′, Y″ are *3d* transition metals with different atomic numbers, X is rare earth and Z is a main-group element). Just as doubling the unit cell yields double structures, tripling it yields triple structures as $X_3Y_3Z_3$ ($Y'Y''_2X_3Z_3$). Double-half Heusler (DHH) alloys with space group I-42d have been proposed by Anand et al. [38]. In order to improve thermoelectric performance, they synthesized the DHH $Ti_2FeNiSb_2$ and claimed that it has a low lattice thermal conductivity. Double half-Heusler compositions $Ti_2FeNiSb_2$, Ti_2Ni_2InSb, and $ScXCo_2Sb_2$ (X = V, Nb, Ta) have had their fundamental characteristics, electronic structure, elastic, optical, and vibrational aspects estimated and investigated within the context of first principle approaches [39,

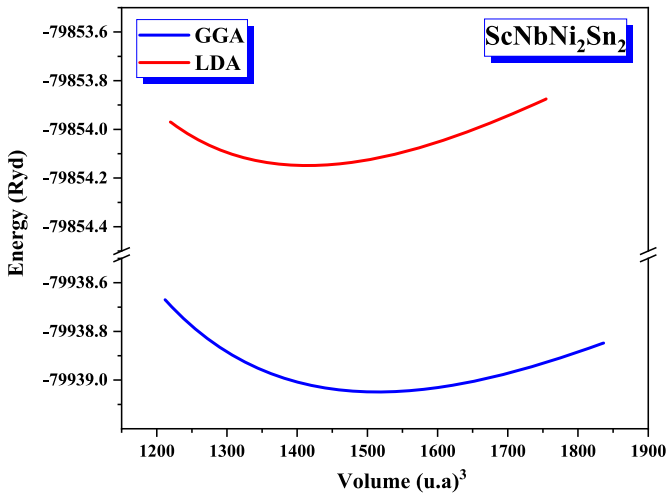

Fig. 2. Total energy as a function of volume for $ScNbNi_2Sn_2$ compound for both GGA and LDA approximations.

40]. Crystals of $ScNb(NiSn)_2$ form a simple orthorhombic structure with the space group *Pmn2₁* (N°31) and have a half-Heusler derivation. This structure is shown in Fig. 1 and this sort of double half-Heusler structure is defined by including two substances with a half-Heusler configuration, each of which has its own distinct crystal geometry. We have fully relaxed the atomic structure (cell parameters) for the purpose of obtaining the fully stable geometric structures of the $ScNb(NiSn)_2$ DHH alloy. Table 1 displays the results of this relaxation in terms of atomic coordinates. We also conduct structural optimizations on the ScNb $(NiSn)_2$ alloy for ferromagnetic (FM) and nonmagnetic (NM) phases in order to establish the equilibrium lattice constant and define the stable structure of the investigated DHH alloy. The Birch-Murnaghan EOS [41] is used to adjust the total energy values as a function of volume using the two approximation LDA and GGA. ScNb(NiSn)2 was shown to have a nonmagnetic (NM) state, as predicted by the computations. The optimized findings for the lattice constant *a*, bulk modulus *B* (GPa), and its first derivative *B′* are shown in Table 2. The optimization of these calculations for our compound reveals that the lowest energy is in the GGA approximation with the nonmagnetic state (see Fig. 2), so it can be concluded that the GGA approximation is the most adequate one to describe the structural properties. For this reason, we will only display the GGA and EV-GGA results in the following subsections.

As shown in Fig. 2, Sc forms 10-coordinate bonds with 4 Ni and 6 Sn atoms. Among the four Sc–Ni bond lengths, three are smaller (2.646 Å) and one is larger (2.758 Å). There are three Sc–Sn lengths of chemical bonds that are smaler (3.0231 Å) and three that are larger (3.049 Å). Distorted face-sharing $NbNi_4Sn_6$ tetrahedra are formed when Nb bonds with 4 Ni and 6 Sn atoms. One Nb–Ni bond length is shorter (2.5005 Å), while three are longer (2.6125 Å) (see Table 2). Three Nb–Sn bond lengths are 3.0259 Å and three are 3.05024 Å. Two Ni sites are non-identical to one another. Ni forms a body-centered cubic connection with 1 Sc, 3 Nb, and 4 Sn atoms in the first Ni site. The shortest Ni–Sn

Table 3
The elastic constants for $ScNbNi_2Sn_2$ computed using GGA.

$ScNbNi_2Sn_2$	
C_{11}	**210.4750 GPa**
C_{22}	**235.4668 GPa**
C_{33}	**234.2404 GPa**
C_{44}	**74.3929 GPa**
C_{55}	**72.3223 GPa**
C_{66}	**72.9843 GPa**
C_{12}	**77.6167 GPa**
C_{13}	**78.0717 GPa**
C_{23}	**90.5160 GPa**

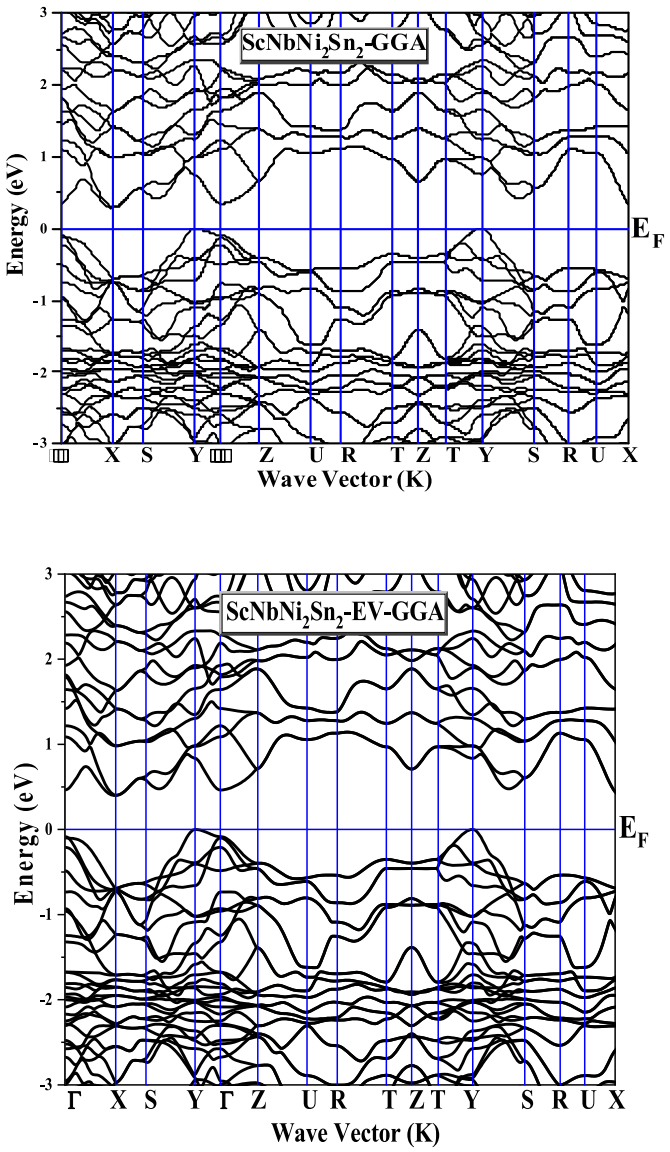

Fig. 3. The band structure along the symmetry lines of the BZ of DHH $ScNbNi_2Sn_2$ using GGA and EV-GGA approximations.

bond length is 2.55 Å, while the three longest are 2.65 Å. When looking at the second Ni site, we see that it is connected to 3 Sc, 1 Nb, and 4 Sn atoms via a body-centered cubic shape. Specifically, three of the Ni–Sn bonds are smaller (2.60 Å) and one is larger (2.72 Å). Both Sn sites are distinct from one another. At the first Sn site, there are 10 coordinates in Sn with 3 Sc, 3 Nb, and 4 Ni atoms. Ten-coordinate bonds connect a second Sn atom to 3 Sc atoms, 3 Nb atoms, and 4 Ni atoms.

To further demonstrate the stability of these compounds, we calculate the elasticity constants Cij using the stress-strain method in the GGA approximation. Nine separate constants (C_{11}, C_{22}, C_{33}, C_{12}, C_{13}, C_{23}, C_{44}, C_{55}, and C_{66}) entirely characterize the elastic behavior of an orthorhombic structure. In Table 3 we show the GGA approximation values for the anisotropic elastic constants of ScNbNi2Sn2 in the orthorhombic structure. Based on these Cij values, it seems this material exhibits

Table 4
Calculated fundamental energy band gaps (*Eg* in eV) of $ScNbNi_2Sn_2$ compound.

$ScNbNi_2Sn_2$	E_g ($Y \rightarrow X$) (eV)				
	GGA	LDA	EV-GGA	mBJ-GGA	mBJ-LDA
	0.373	0.382	0.470	0.379	0.388

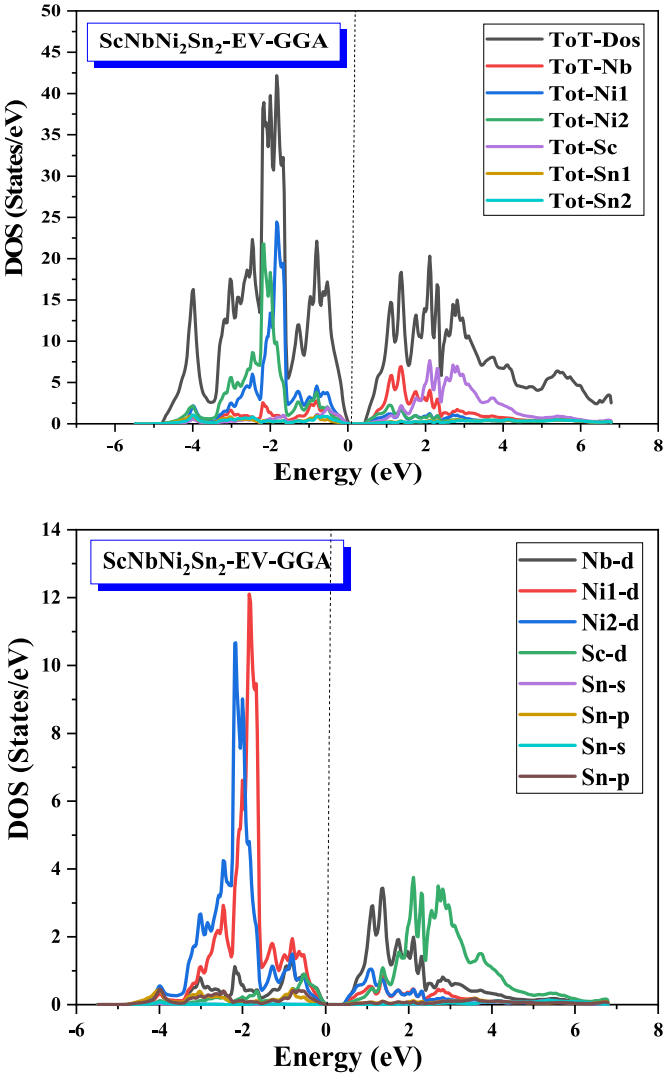

Fig. 4. Orbital electronic density of states for $ScNbNi_2Sn_2$ compound using EV-GGA approximation.

elastic anisotropy. In Table 3 we show the GGA approximation values for the anisotropic elastic constants of $ScNbNi_2Sn_2$ in the orthorhombic structure. Based on these Cij values, it seems this material exhibits elastic anisotropy. ScNbNi2Sn2 has a stiffer orthorhombic structure in the [010] direction than in the [001] or [100] directions ($C_{22}>C_{33}>C_{11}$). Mechanical stability of the $Pmn2_1$ structure of $ScNbNi_2Sn_2$ is indicated by the values of the elastic constants determined at 0 GPa with GGA, which confirm all the stability conditions stated in equation (1).

$$C_{11} > 0, C_{22} > 0, C_{33} > 0, C_{44} > 0, C_{55} > 0, C_{66} > 0, [C_{11} + C_{22} - 2C_{12}] > 0,$$
$$[C_{11} + C_{33} - 2C_{13}] > 0, [C_{22} + C_{33} - 2C_{23}] > 0, C_{11} + C_{22} + C_{33} + 2\ [C_{12} + C_{13} + C_{23}] > 0, \quad (1)$$
$$\frac{1}{3}\ [C_{12} + C_{13} + C_{23}] < B < \frac{1}{3}\ [C_{11} + C_{22} + C_{33}]$$

3.2. Electronic structure

The valence and conduction band electron distributions are the primary determinants of the electronic features, band structure, and state density, we have calculated these properties of DHH $ScNbNi_2Sn_2$ in their equilibrium condition with their lattice parameter optimized. The band structure of $ScNbNi_2Sn_2$ was obtained using GGA, mBJ-GGA, LDA, mBJ-LDA, and EV-GGA approximations. Fig. 3 shows that the X point is the minimum of the conduction band (CBM) in $ScNbNi_2Sn_2$, and that the Y point is the maximum of the valence band (VBM) in the first *Brillouin Zone*, establishing that $ScNbNi_2Sn_2$ is a semiconductor and displays an indirect bandgap equal tõ0:47 eV with EV-GGA which gives us the best bandgap value according to Table 4.

The total and partial density of states of the DHH $ScNbNi_2Sn_2$ alloy at his equilibrium lattice constant have been computed using the GGA, mBJ-GGA, LDA, mBJ-LDA, and EV-GGA approximations, providing us with insight into the genesis of the electronic structure in our semiconductor. Fig. 4 represents to total and partial density of states (DOS). Valence bands emerge between −4.8 eV and E_F in the plot DOS around the *Fermi* level, which is due mostly to the biggest contributions of *d*-orbitals of Ni atoms. Sn contributions are negligible while the rest orbitals of Sc and Nb atoms have small contributions. Due to the modest contribution of the *d*-orbitals of Nb and Sc, there is simple predominance of the conduction band within the energy ranges of 0.47 eV and 6.9 eV. All other atoms' rest orbitals, on the other hand, are extremely small in

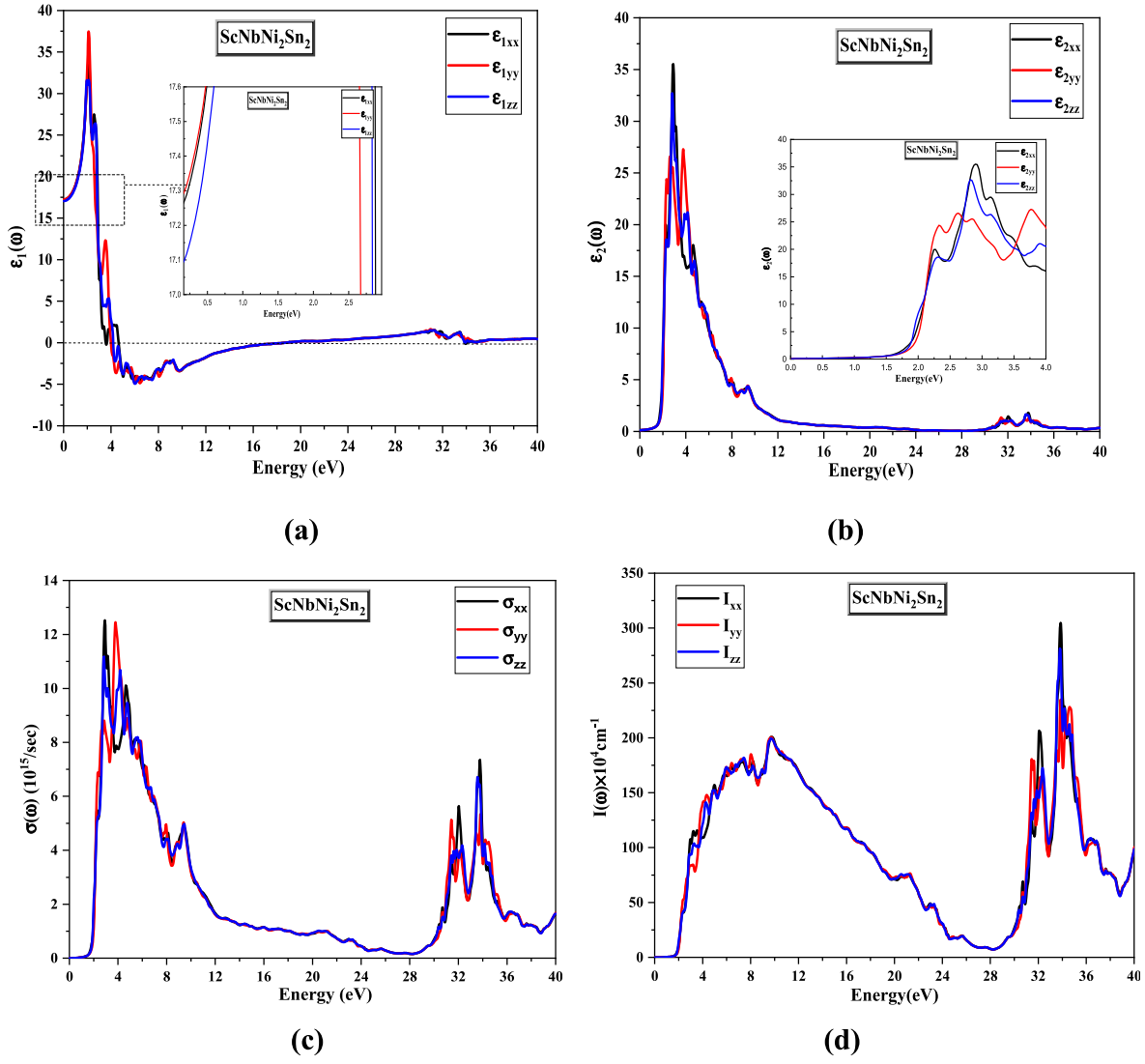

Fig. 5. Variation of **(a)** the real part ε_1, **(b)** the imaginary part of the dielectric function, **(c)** electrical conductivity, and **(d)** absorption coefficient.

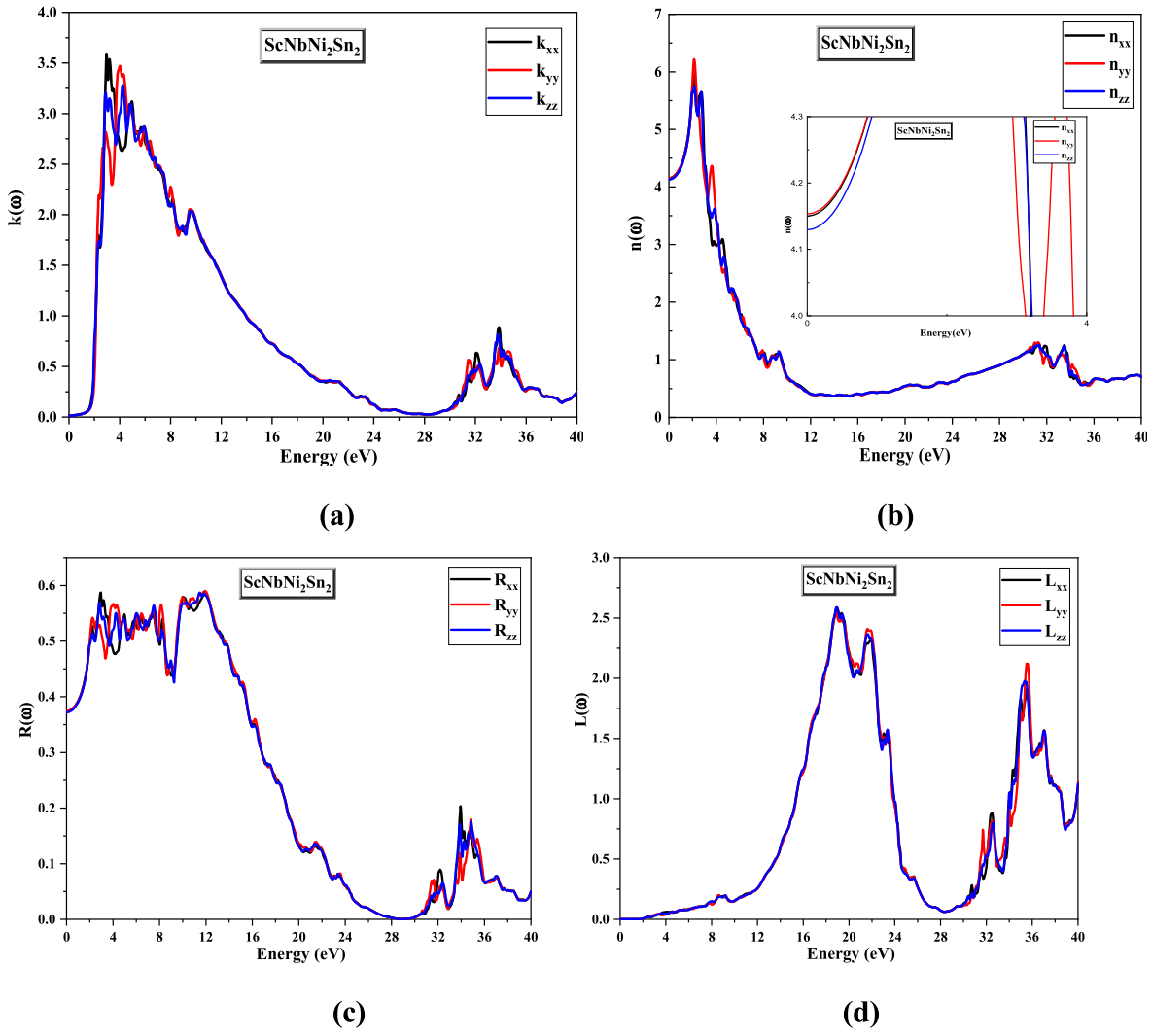

Fig. 6. Optical spectra as a function of photon energy for $ScNbNi_2Sn_2$ within EV-GGA approximation: **(a)** the extinction coefficient, **(b)** the refractive index, **(c)** reflectivity spectra, and **(d)** the energy loss function.

comparison.

3.3. Optical properties

We have computed in this subsection, the optical characteristics along the x, y, and z axes from 0 to 40 eV, including the dielectric function variation $\varepsilon(\omega)$, the optical conductivity $\sigma(\omega)$, the refractive index $n(\omega)$, the extinction $k(\omega)$, the absorption $I(\omega)$ and reflection coefficients $R(\omega)$, and the energy loss spectrum $L(\omega)$ for $ScNbNi_2Sn_2$ using EV-GGA approximation.

The complex dielectric function demonstrates how the optical properties of a material are affected by the incident wavelength of light and can be defined as:

$$\varepsilon(\omega) = \varepsilon_1(\omega) + i\varepsilon_2(\omega) \tag{2}$$

where ε_2 represents the imaginary part, and the following formula depicts it

$$\varepsilon_2(\omega) = \frac{qe^2\hbar}{\pi m^2\omega^2}\sum_{V,C}\int_{BZ}|M_{CV}(k)|^2\delta[\omega_{CV}(k)-\omega]d^3k \tag{3}$$

with q is the charge of the electron and m is the mass.

$$M_{CV}(k) = \langle u_{ck}|e\nabla|u_{ck}\rangle \tag{4}$$

$M_{CV}(k)$ represents the matrix elements for the transitions between valence and conduction band with e the polarization vector of the electric field.

$$\omega_{CV}(\omega) = E_{CK} - E_{VK} \tag{5}$$

$\omega_{CV}(\omega)$ is the energy of excitement.

On the other side $\varepsilon_1(\omega)$ represents the real part of the dielectric function can be obtained from the imaginary part Kramers-Kroning relation [42]:

$$\varepsilon_1(\omega) = 1 + \frac{2}{\pi}P\int_0^{\infty}\frac{\omega'\varepsilon_2(\omega')}{\omega^2-\omega^2}d\omega' \tag{6}$$

P represents the main value of the integral.

The absorption coefficient $I(\omega)$ is presented as:

$$I(\omega) = \frac{2\pi}{\lambda}\,\mathrm{k}(\omega) \tag{7}$$

Where λ represents the wavelengths of the light in a vacuum.

The refractive index depends on the frequency of the light beam.

$$n(\omega) = \left[\frac{\varepsilon_1(\omega)}{2} + \frac{\sqrt{\varepsilon_1{}^2(\omega)+\varepsilon_2{}^2(\omega)}}{2}\right]^{1/2} \tag{8}$$

Table 5
Calculated $\varepsilon_1(0)$, $n(0)$, $R(0)$, and $L(0)$ $ScNbNi_2Sn_2$ compound within GGA, mBJ-GGA, LDA, mBJ-LDA, and EV-GGA.

$ScNbNi_2Sn_2$	$\boldsymbol{\varepsilon_1(0)}$			$\boldsymbol{n(0)}$			$\boldsymbol{R(0)}$			$\boldsymbol{L(0)}$		
Approximations	ε_{1xx}	ε_{1yy}	ε_{1zz}	n_{xx}	n_{yy}	n_{zz}	R_{xx}	R_{yy}	R_{zz}	L_{xx}	L_{yy}	L_{zz}
GGA	**17.6755**	**17.6611**	**17.4793**	**4.2042**	**4.2025**	**4.1808**	**0.3790**	**0.3789**	**0.3769**	**0.3896x10^{-4}**	**0.3861x10^{-4}**	**0.39016x10^{-4}**
EV GGA	**17.2252**	**17.2534**	**17.0558**	**4.1503**	**4.1537**	**4.1298**	**0.3741**	**0.3744**	**0.3722**	**0.3954x10^{-4}**	**0.3925x10^{-4}**	**0.3962x10^{-4}**
mBJ GGA	**18.0074**	**17.9752**	**17.8159**	**4.2435**	**4.2397**	**4.2209**	**0.3826**	**0.3823**	**0.3806**	**0.3928x10^{-4}**	**0.3897x10^{-4}**	**0.3937x10^{-4}**
LDA	**17.3615**	**17.3581**	**17.1902**	**4.1667**	**4.1663**	**4.1461**	**0.3756**	**0.3756**	**0.3737**	**0.3815x10^{-4}**	**0.3777x10^{-4}**	**0.3819x10^{-4}**
mBJ LDA	**17.5958**	**17.5837**	**17.4184**	**4.1947**	**4.1933**	**4.1735**	**0.3782**	**0.3780**	**0.3662**	**0.3857x10^{-4}**	**0.3821x10^{-4}**	**0.3865x10^{-4}**

The extinction coefficient $k(\omega)$ and the reflection coefficient $R(\omega)$ are given by the following relations:

$$k(\omega) = \left[-\frac{\varepsilon_1(\omega)}{2} + \frac{\sqrt{\varepsilon_1{}^2(\omega) + \varepsilon_2{}^2(\omega)}}{2} \right]^{1/2} \tag{9}$$

$$R(\omega) = \frac{n + ik - 1}{n + ik + 1} \tag{10}$$

The influence of photon energy on the x, y, and z components of the estimated dielectric functions $\varepsilon_1(\omega)$ and $\varepsilon_2(\omega)$ is shown in Fig. 5 (a) and (b). The calculated static value for the real part $\varepsilon_1(\omega)$ of dielectric function for $ScNbNi_2Sn_2$ along the three crystallographic directions is found to be 17.2252 for $\varepsilon_{1xx}(0)$, 17.2534 for $\varepsilon_{1yy}(0)$ and 17.0558 for $\varepsilon_{1zz}(0)$, respectively. The average static value $\varepsilon_1(0)$ is 17.1781. As we can see in Fig. 5. (a) from the zero frequency limit they start increasing and reach the maximum value of 34.06 for $\varepsilon_{1xx}(\omega)$, 37.46 for $\varepsilon_{1yy}(\omega)$ at 2.108 eV, and 31.63 for $\varepsilon_{1zz}(\omega)$ at 2.13 eV, respectively. After that they start decreasing. furthermore, in addition under the energy ranges shifting from 4.7 to 18.7 eV $ScNbNi_2Sn_2$ demonstrates metallic behavior because $\varepsilon_1(\omega)$ is negative, as a result of our compound's ability to reflect incident photon radiant energy in this area.

From Fig. 5. (b) there is strong absorption in the energy range 2.19–4.83 eV. The absorption peak value is 35.52 for $\varepsilon_{2xx}(\omega)$, 27.28 for $\varepsilon_{2yy}(\omega)$, and 32.70 for $\varepsilon_{2zz}(\omega)$ at 2.89 eV, 3.76 eV, and 2.81 eV respectively, which indicates that $ScNbNi_2Sn_2$ is anisotropic.

The optical conductivity $\sigma(\omega)$ is shown in Fig. 5. (c), it begins to increase at 1.5 eV and develops to the value of 12.52 at 2.92 eV for $\sigma_{xx}(\omega)$,12.45 at 3.79 eV for $\sigma_{yy}(\omega)$, and 11.18 at 2.84 eV for $\sigma_{zz}(\omega)$ then it gradually decreases until it reaches 28 eV. After that it increases again with the appearance of other medium peaks up to 40 eV.

The absorption coefficient $I(\omega)$ from Fig. 5. (d) starts from the energy 1.5 eV, in which the absorption begins to increase until reaching the value of about 200.909×10^4 Cm^{-1} at an energy range of 9.72 eV then it begins to increase again to arrive at an extremely intense about 304 at 34 eV along the *x* axe.

In Fig. 6. (a), the extinction coefficient $k(\omega)$ reflects the maximum absorption in the medium at 2.95 eV for $k_{xx}(\omega)$,4 eV for $k_{yy}(\omega)$, and 4.23 eV for $k_{zz}(\omega)$ with average value 3.43. The refractive index is shown in Fig. 6. (b) from the plot $n(\omega)$ emerges from 4.1503, 4.1537 and 4.1298 for n_{xx} (0), n_{yy} (0), and n_{zz} (0) directions respectively. So, the average value of $n(0)$ is equal to 4.1446 and it is obtained from the real part of the dielectric function to be $n(0) = \sqrt{\varepsilon_1(0)} = \sqrt{17.1781} = 4.1446$ (see Table 5) and arrives to a highest value 5.94, 6.21, and 5.73 for n_{xx}, n_{yy}, and n_{zz} directions respectively, at 2.13 eV energy. It then begins to decline with multiple, smaller peaks and continues to decline up to 20 eV and it begins to rise slightly forming very small peaks at the end of the energy range.

Fig. 6 (c) defines the reflectance variation of $ScNbNi_2Sn_2$, at the zero frequency the value of the reflectance is about 37.3% where the greatest value emerges at 57.3% in the energy range 2.83–8.47 eV. The variation of the energy loss spectrum function is shown in Fig. 6. (d) the peaks correspond to the plasma resonance and the corresponding frequencies called the resonant energy loss occur at an energy of 18.92 eV and 35.5 eV for all directions.

3.4. Thermoelectric features

3.4.1. Lattice thermal conductivity

To quantify the effectiveness of thermoelectric power production, scientists use a metric known as the figure of merit $ZT = \frac{\sigma S^2 T}{k_e + k_L}$ where S is the material's Seebeck coefficient, σ is its electrical conductivity, T is its absolute temperature, and k_e and k_L are its electronic and lattice thermal conductivities. Low lattice thermal conductivity is required for promising thermoelectric materials. The total thermal conductivity ($\kappa_{Tot} = \kappa_e + \kappa_L$) is the sum of the lattice thermal conductivity κ_L and electronic thermal conductivity κ_e. The slacks equation is a standard approximation for calculating lattice thermal conductivity [43,44].

Slack's equation was utilized to determine the lattice thermal conductivity k_L, while the BoltzTraP algorithm was utilized to evaluate the electronic thermal conductivity k_e. We estimated the Debye temperature utilizing a quasi-harmonic Debye model incorporated in the original Gibbs software [45–48].

We have used the constant relaxation time approximation $\tau = 3 \times 10^{-14}$ s, in the temperatures range from 50 K to 1000 K are considered in our calculations. How temperature affects k_L is seen in Fig. 7 (a). $ScNbNi_2Sn_2$ is predicted to have lattice k_L values between 5.3070 W K^{-1} m^{-1} (at 300 K) and 1.3465 W K^{-1} m^{-1} (at 1000 K). As temperature increases, there is an increase in phonon vibrations, leading to a considerable decrease in the value of k_L. So, compounds are thought to be promising candidates for usage as excellent thermoelectric materials because of their low lattice thermal conductivities. Considering this, it is necessary to look at the transportation options available. Fig. 7 (b) shows that, on the other hand, ke rises as a function of temperature. Wiedemann and Franz's formulation gives an account of how k_e and σ are related ($k_e = \sigma LT$), where L stands for the Lorentz number. As seen in Fig. 7 (c), k_{Tot} continues to decrease with increasing temperature until T exceeds 400 K. When this happens, the trend begins to reverse. The value of roughly 6,0284 W/(m.K) is derived based on the comparatively low thermal conductivity at 400 K.

3.4.2. Transport parameters

The transport coefficients (σ, S, and k_e) of the $ScNbNi_2Sn_2$ compound may be determined using the relaxation time assumption, they can be expressed as [49–52]:

$$\sigma = e^2 \sum_k \left(-\frac{\partial f_0}{\partial E} \right) \tau_{\overrightarrow{k}} v_{\overrightarrow{k}} v_{\overrightarrow{k}} \tag{11}$$

Where σ is the electrical conductivity, f_0 is a *Fermi* distribution function, $\tau_{\overrightarrow{k}}$ and $v_{\overrightarrow{k}}$ signify the relaxation time and the group velocity associated with $\overrightarrow{k}$ state, respectively. It can be shown that the Seebeck coefficient can be calculated using

$$S = eK_B\sigma^{-1} \sum_k \left(-\frac{\partial f_0}{\partial E} \right) \tau_{\overrightarrow{k}} v_{\overrightarrow{k}} v_{\overrightarrow{k}} \left(\frac{\varepsilon_k - \mu}{K_B T} \right) \tag{12}$$

Where ε_k is the band energy, μ is the chemical potential. The definition of the electronic contributions to thermal conductivity is:

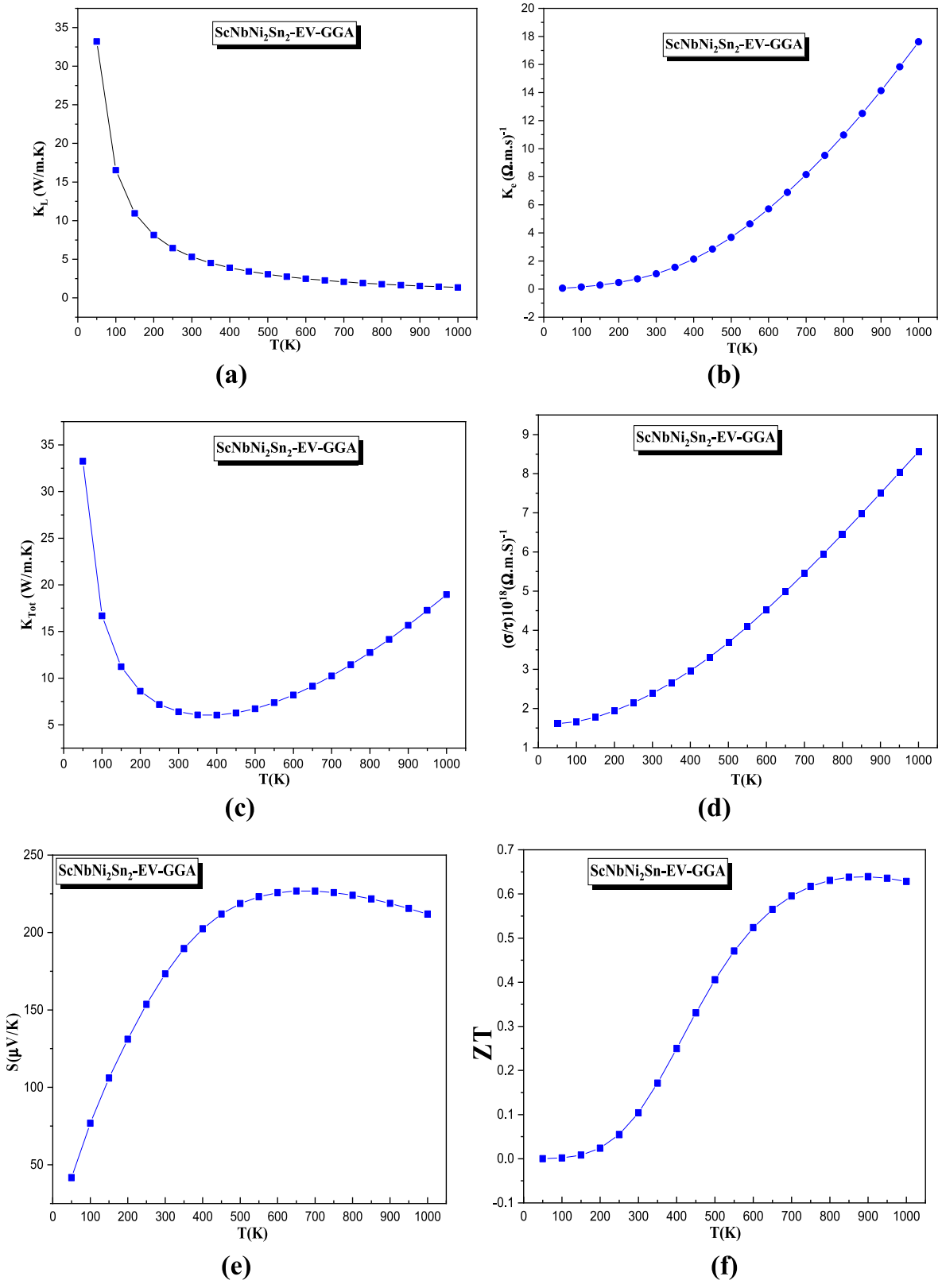

Fig. 7. Temperature dependency of **(a)** the thermal conductivity of the lattice k_L,**(b)** thermal conductivity of electronics k_e,**(c)** the total thermal conductivity k_{Tot}, **(d)** the electrical conductivity per relaxation time (σ/τ), **(e)** the coefficient of Seebeck S, **(f)** the figure of merit ZT of $ScNbNi_2Sn_2$ according to the EV-GGA approximation.

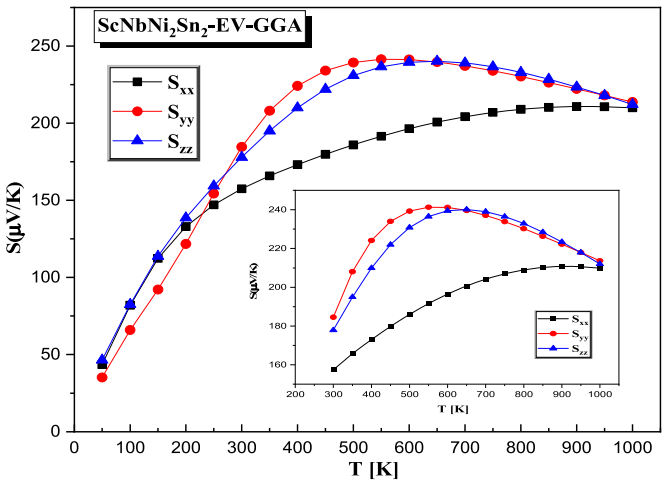

(a)

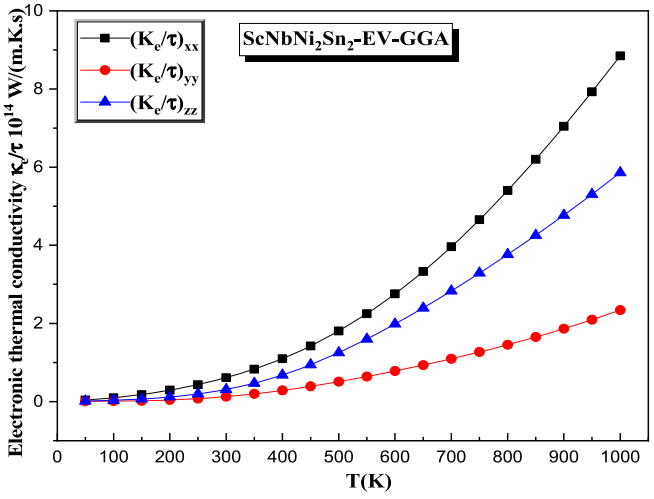

(b)

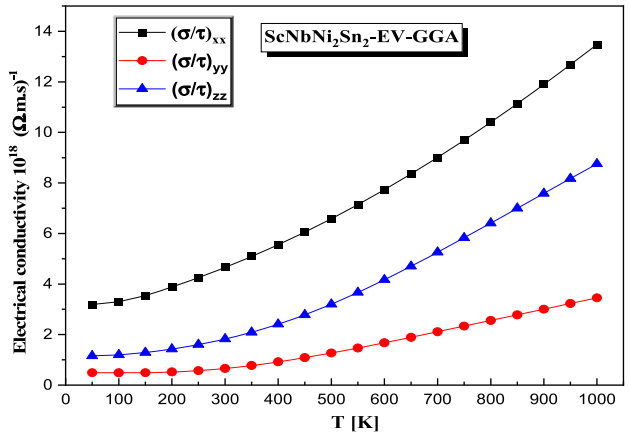

(c)

Fig. 8. Calculated anisotropic transport properties of $ScNbNi_2Sn_2$ compound **(a)** Seebeck coefficient tensor **(b)** electronic thermal conductivity tensor and **(c)** ratio of electrical conductivity tensor components.

Table 6
The calculated of the Seebeck coefficient tensor of $ScNbNi_2Sn_2$ at 300 K and 1000 K, using EV-GGA approximation.

Compound	T(K)	S_{xx} (μV/K)	S_{yy} (μV/K)	S_{zz} (μV/K)
$ScNbNi_2Sn_2$	1000	209.90	213.70	212.03
	300	157.43	184.56	177.89
	S_{max}	210.73 (900 K)	241.32 (600 K)	240.15 (650 K)

Table 7
The calculated electrical conductivity tensor of $ScNbNi_2Sn_2$ at 300 K and 1000 K, using EV-GGA and GGA approximations.

Compound	Approximations	T(K)	$\sigma*10^{18}(W.m.S)^{-1}$		
			σ_{xx}	σ_{yy}	σ_{ZZ}
$ScNbNi_2Sn_2$	**EV-GGA**	**1000**	**13.47**	**3.45**	**8.75**
		300	**4.66**	**0.65**	**1.82**
	GGA	**1000**	**13.02**	**3.30**	**8.08**
		300	**4.47**	**0.56**	**1.58**

$$k_e = K_B^2 T \sum_k \left(-\frac{\partial f_0}{\partial E} \right) \tau_{\overrightarrow{k}} v_{\overrightarrow{k}} v_{\overrightarrow{k}} \left(\frac{\varepsilon_k - \mu}{K_B T} \right)^2 - T\sigma S^2 \quad (13)$$

Wiedemann-Franz equation is also useful for determining the electronic thermal conductivity parts [53], L is the Lorentz number

$$K_e = LT\sigma \quad (14)$$

In Fig. 7 (d), as the temperature increases, so does the electrical conductivity as measured by the relaxation time (σ/τ) of $ScNbNi_2Sn_2$. It seems to vary linearly with temperature, as expected by the band structure analysis, and so confirms the semiconducting property. $ScNbNi_2Sn_2$ was found to have a (σ/τ) of $2.3823*10^{18}$ $(\Omega ms)^{-1}$ at a temperature of 300 K. The value of $8.5611*10^{18}$ $(\Omega ms)^{-1}$ was determined at a temperature of 1000 K.

Coefficients of Seebeck S of double half-Heuslers alloys is influenced by the electronic band structure of the alloys. Evaluation of the material's capacity to generate a voltage in reaction to a change in temperature. S of $ScNbNi_2Sn_2$ has been seen to rise with temperature until 750 K, after which the tendency reverses. Fig. 7 (e) demonstrates that the values of S for $ScNbNi_2Sn_2$ grow from 173.2968 V K^{-1} at 300 K to 211.8817 V K^{-1} at 1000 K, indicating that S is continuously positive across the whole temperature range. Given that S is positively charged, holes are projected to be the principal charge carriers in $ScNbNi_2Sn_2$ material, which plays a crucial role in conduction. $ScNbNi_2Sn_2$ is a p-type compound because, regardless of temperature, its S value is always positive.

The ZT phenomenon is comparable to that of electrical conductivity. ZT rises as a function of temperature (as predicted, as seen in Fig. 7(f)) up to around T = 900 K, after which it decreases. As the temperature rises from 600 K to 900 K, the ZT values rise from 0.5237 to 0.6391.

RbCrC has a ZT of 0.94 at 800 K [54], ZT equal to 0.73 at 300 K for *RhTiSb* [55], n-type of $Bi_2Al_4Se_8$ has ZT value off 0.76 when n equal to -$6.448*10^{18}$ cm^3 [56], at T = 700 K (T = 810 K) $ZT = 0.5$ (ZT = 0.1) for *VCoSb* (*ScNiSb*) [57,58], ZT~ 0.99 (*CuPN*$_2$: $n = -1.7$ $*10^{19} cm^3$) for n-type, (*HPN*$_2$: $n = 1.4$ $*10^{19} cm^3$) for p-type, (*LiPN*$_2$ or *NaPN*$_2$, $n = 0.4*10^{19} cm^3$) for p-type [59,60], and at 700 K $CaZn_2Sb_2$ has ZT of 0.33 [61]. For n-type of *LiCrZ* (Z = *S, Se, Te*), ZT equal to 0.68, 0.9495, and 0.9507 when $n = -97.77*10^{21}$ cm^3, $n = -84.85*10^{21}$ cm^3, and $n = 67.48*10^{21}$ cm^3, respectively [62]. For *CoFeTiGe* (*CoFeCrGe*), ZT = 0.25 and 0.404 (0.243 and 0.644) for n and p-*type*, respectively, when $n = -5.75*10^{20}$ cm^3 and $n = 18.61*10^{21}$ cm^3 ($n = -10.83*10^{20}$ cm^3 and $n = 60.52*10^{21}$ cm^3), respectively [63].

After demonstrating the strong thermoelectric performance of $ScNbNi_2Sn_2$, we calculate (S, (σ/τ), (k_e/τ)) along the x, y, and z axes using the EV-GGA method. Tensors $(\sigma_{xx} \neq \sigma_{yy} \neq \sigma_{zz})$, $(S_{xx} \neq S_{yy} \neq S_{zz})$, $(k_{e_{xx}} \neq k_{e_{yy}} \neq k_{e_{zz}})$ are diagonal.

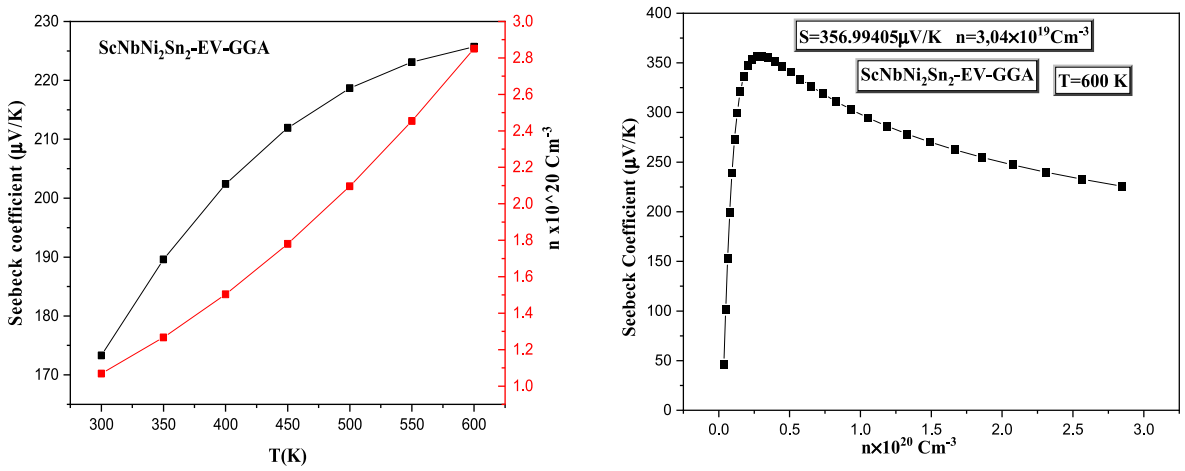

Fig. 9. Enhancing the Seebeck coefficient of double half heusler $ScNbNi_2Sn_2$ as function of the temperature range 300 K–600 K and carrier concentrations.

In the temperature range of 50–250 K, as shown in Fig. 8 (a), the S_{zz} Seebeck coefficient has larger values than the S_{xx} tensor, but this trend is inverted at T = 300–600 K, where the S_{yy} tensor has higher values than the *zz* and *xx* tensors. In the subsequent interval, between T = 650 K and 1000 K, S_{zz} is the most dominant. From Table 6, the Seebeck coefficient value S_{yy} is higher than that found in S_{xx} and S_{zz} at T = 300 and 1000 K. In particular, at T = 300 K (S_{xx} = 157.43 μ V/K S_{yy} = 184.56 μ V/K, S_{zz} = 177.89 μV/K). The large values of S_{yy} indicates the dominance of transport along the *yy* axis. The highest value of all tensors has been found to be along the axes *yy*, because S_{yy} in approximation EV-GGA reaches values of 241.32 $\mu V/K$ at (600 K) which indicates that the transport is dominated by the *yy*-axis. $(K_{e_{xx}}/\tau)$ is greater than $(K_{e_{zz}}/\tau)$ and $(K_{e_{yy}}/\tau)$ besides that when T = 600 K, $(K_{e_{zz}}/\tau)$ is 71% of $(K_{e_{xx}}/\tau)$ and $(K_{e_{yy}}/\tau)$ is 28% of $(K_{e_{xx}}/\tau)$ (Fig. 8 (b)). In addition, at elevated temperatures, the disparity between these three characteristics becomes more significant. T = 900 K at elevated temperatures (σ_{zz}/τ) is 63% of (σ_{xx}/τ) whereas (σ_{yy}/τ) is only 25% of (σ_{xx}/τ), it is supported by the significant concentration of states in this direction (Fig. 8 (c)). So, the electrical conductivity is dominated by the *xx*-axis in temperature range between 50 K and 1000 K. All the calculated electrical conductivity tensors along the axes *xx*, *yy*, and *zz* for temperature equal to 300 K and 1000 K using the two approximations GGA and EV-GGA are presented in Table 7.

3.4.3. Seebeck coefficient enhancing

Fig. 9 shows how the Seebeck coefficient varies with the temperature range 300 K–600 K of double half heusler $ScNbNi_2Sn_2$. At 600 K the value of *S* is 225.70 μV/K corresponding to a carrier concentration of $n = 28.50 \times 10^{19}Cm^{-3}$ within EV-GGA and 228.875 μV/K corresponding to a carrier concentration of $n = 24 \times 10^{19}Cm^{-3}$ within GGA. We have also studied in both approximation GGA and EV-GGA the effect of the carrier concentration on the Seebeck coefficnet at T = 600 K. The maximum value of *S* is 281.8747 μV/K with $n = 6.9 \times 10^{19}Cm^{-3}$ and 356.9905 μV/K with $n = 3.04 \times 10^{19}Cm^{-3}$ within GGA and EV-GGA respectively.

4. Conclusion

We have studied the structural, electronic, optical, and thermoelectric properties of the DHH compound $ScNbNi_2Sn_2$ employing DFT implemented in the Wien2k code. Our results can be summarized as follows:

The study of structural properties shows that $ScNbNi_2Sn_2$ crystallizes in the simple orthorhombic $Pmn2_1$ space group, the result of the lattice constants within GGA approximation *a*, *b*, and *c* are 4.287 Å, 8.606 Å, and 6.074 Å. The energy of the ground state E_{min}, compressibility modulus *B*, and pressure derivative B' of the $ScNbNi_2Sn_2$ compound are reported in this work for the first time.

According to the electronic properties our compound is a semiconductor and has an indirect $(Y \rightarrow X)$ narrow bandgap = 0.47 eV using EV-GGA approximation. Using the EV-GGA approach we have investigated the optical properties and we concluded that our material is a good choice for optoelectronic devices. Finally, the effects of temperature on thermoelectric parameters are investigated using BoltzTraP code we have calculated the most important properties which are transport properties such as the Seebeck coefficient, it has a positive value which indicates that $ScNbNi_2Sn_2$ is (*p*-type) semiconductor. We have also calculated other parameters such as electrical, thermal conductivities, and ZT. As the temperature rises from 600 K to 900 K, the ZT values rise from 0.5237 to 0.6391. We calculated (*S*, (σ/τ), (k_e/τ)) along the *x*, *y*, and *z* axes using the EV-GGA method. We found out that our compound is thermoelectrically anisotropic. We have also studied in both approximation GGA and EV-GGA the effect of the carrier concentration on the Seebeck coefficnet at T = 600 K. The maximum value of *S* is 281.8747 μV/K with $n = 6.9 \times 10^{19}Cm^{-3}$ and 356.9905 μV/K with $n = 3.04 \times 10^{19}Cm^{-3}$ within GGA and EV-GGA respectively.

Credit author statement

H. Mekki, Writing – original draft preparation, **H. Baaziz**, Supervision; Methodology, Writing – review & editing, **Z.Charifi**, Writing – original draft, Writing – review & editing,**T. Ghellab** Writing – review & editing, **A. E. Genç**;, Data curation, Formal analysis, **Ş. Uğur** Investigation, Methodology, **G. Uğur** Writing – review & editing

Declaration of competing interest

The authors declare that they have no known competing financial interests or personal relationships that could have appeared to influence the work reported in this paper.

Data availability

Data will be made available on request.

Acknowledgments

The authors (H. Mekki, H. Baaziz, Z. Charifi, and T. Ghellab) would like to thank the general directorate for scientific research and technological development for their financial support during the realization of this work.

References

[1] W.G. Zeier, J. Schmitt, G. Hautier, U. Aydemir, Z.M. Gibbs, C. Felser, G.J. Snyder, Nat. Rev. Mater. 1 (2016), 16032.
[2] T. Zhu, Y. Liu, C. Fu, J.P. Heremans, J.G. Snyder, X. Zhao, Adv. Mater. 29 (2017), 1605884.
[3] J. Mao, Z. Liu, J. Zhou, H. Zhu, Q. Zhang, G. Chen, Z. Ren, Adv. Phys. 67 (2018) 69–147.
[4] C. Fu, S. Bai, Y. Liu, Y. Tang, I.L. Chen, X. Zhao, T. Zhu, Nat. Commun. 6 (2015) 8144.
[5] H. Zhu, J. Mao, Y. Li, J. Sun, Y. Wang, Q. Zhu, G. Li, Q. Song, J. Zhou, Y. Fu, et al., Nat. Commun. 10 (2019) 270.
[6] H. Zhu, R. He, J. Mao, Q. Zhu, C. Li, J. Sun, W. Ren, Y. Wang, Z. Liu, Z. Tang, et al., Nat. Commun. 9 (2018) 2497.
[7] S. Sakurada, N. Shutoh, Appl. Phys. Lett. 86 (8) (2005), 082105.
[8] G. Rogl, P. Sauerschnig, Z. Rykavets, V. Romaka, P. Heinrich, B. Hinterleitner, A. Grytsiv, E. Bauer, P. Rogl, Acta Mater. 131 (2017) 336–348.
[9] J. Zhou, H. Zhu, T.-H. Liu, Q. Song, R. He, J. Mao, Z. Liu, W. Ren, B. Liao, D. J. Singh, et al., Nat. Commun. 9 (2018) 1721.
[10] Y. Pei, X. Shi, A. LaLonde, H. Wang, L. Chen, G.J. Snyder, Nature 473 (2011) 66–69.
[11] J.P. Heremans, V. Jovovic, E.S. Toberer, A. Saramat, K. Kurosaki, A. Charoenphakdee, S. Yamanaka, G.J. Snyder, Science 321 (2008) 554–557.
[12] A. Romero, E. Gross, M. Verstraete, O. Hellman, Phys. Rev. B 91 (2015), 214310.
[13] M. Wood, U. Aydemir, S. Ohno, G.J. Snyder, J. Mater. Chem. A Mater. Energy Sustain. 6 (20) (2018) 9437–9444.
[14] G. Tan, S. Hao, R.C. Hanus, X. Zhang, S. Anand, T.P. Bailey, A.J. Rettie, X. Su, C. Uher, V.P. Dravid, et al., ACS Energy Lett. 3 (2018) 705–712.
[15] E.S. Toberer, A. Zevalkink, G.J. Snyder, J. Mater. Chem. 21 (2011) 15843–15852.
[16] M.R. Winter, D.R. Clarke, J. Am. Ceram. Soc. 90 (2007) 533–540.
[17] E.S. Toberer, C.A. Cox, S.R. Brown, T. Ikeda, A.F. May, S.M. Kauzlarich, G. J. Snyder, Adv. Funct. Mater. 18 (2008) 2795–2800.
[18] S. Vasala, M. Karppinen, Prog. Solid State Chem. 43 (2015) 1–36.
[19] M.T. Anderson, K.R. Poeppelmeier, Chem. Mater. 3 (3) (1991) 476–482.
[20] P. Kanhere, Z. Chen, Molecules 19 (2014) 19995–20022.
[21] J. Kangsabanik, V. Sugathan, A. Yadav, A. Yella, A. Alam, Phys. Rev. Mater. 2 (2018), 055401.
[22] K.-I. Kobayashi, T. Kimura, H. Sawada, K. Terakura, Y. Tokura, Nature 395 (1998) 677–680.
[23] S. Anand, K. Xia, V.I. Hegde, U. Aydemir, V. Kocevski, T. Zhu, C. Wolverton, G. J. Snyder, Energy Environ. Sci. 11 (2018) 1480.
[24] A. Page, A. Van der Ven, P. Poudeu, C. Uher, J. Mater. Chem. A Mater. Energy Sustain. 4 (2016) 13949–13956.
[25] R. Gautier, X. Zhang, L. Hu, L. Yu, Y. Lin, T.O. Sunde, D. Chon, K.R. Poeppelmeier, A. Zunger, Nat. Chem. 7 (2015) 308–316.
[26] T. Graf, C. Felser, S.S. Parkin, Prog. Solid State Chem. 39 (2011) 1–50.
[27] F. Yan, X. Zhang, Y.G. Yu, L. Yu, A. Nagaraja, T.O. Mason, A. Zunger, Nat. Commun. 6 (2015) 7308.
[28] J. Ma, V.L. Hegd, K. Munira, Y. Xie, S. Keshavarz, D.T. Mildebrath, C. Wolverton, A. W. Ghosh, W. Butler, Phys. Rev. B 95 (2017), 024411.
[29] S. Anand, K. Xia, T. Zhu, C. Wolverton, G.J. Snyder, Adv. Energy Mater. 8 (2018), 1801409.
[30] W. Kohn, L.J. Sham, Phys. Rev. 140 (4A) (1965) A1133.
[31] P. Blaha, K. Schwarz, G.K.H. Madsen, D. Kvasnicka, J. Luitz, WIEN2k, an Augmented Plane Wave Plus Local Orbitals Program for Calculating Crystal Properties, Vienna University of Technology, Vienna, 2001.
[32] P. Hohenberg, W. Kohn, Phys. Rev. 136 (1964) B864.
[33] J.P. Perdew, K. Burke, M. Ernzerhof, Phys. Rev. Lett. 77 (1996) 3865.
[34] J.P. Perdew, Y. Wang, Phys. Rev. B 45 (1992), 13244.
[35] F. Tran, P. Blaha, Phys. Rev. Lett. 102 (2009), 226401.
[36] E. Engel, S.H. Vosko, Phys. Rev. B 47 (1993), 13164.
[37] G.K.H. Madsen, D.J. Singh, Comput. Phys. Commun. 175 (2006) 67.
[38] S. Anand, M. Wood, Y. Xia, C. Wolverton, G.J. Snyder, Joule 3 (5) (2019) 1226–1238.
[39] Z. Charifi, H. Baaziz, Ş. Uğur, G. Uğur, Indian J. Phys. (2022) 1–16.
[40] G. Uğur, A.K. Kushwaha, M. Güler, Z. Charifi, Ş. Uğur, E. Güler, H. Baaziz, Mater. Sci. Semicond. Process. 123 (2021), 105531.
[41] F.D. Murnaghan, Proc. Natl. Acad. Sci. USA 30 (9) (1944) 244–247.
[42] H.A. Kramers, *Atti Cong. Intern. Fisica* (*Transactions of Volta Centenary Congress, Como*) 2 (1927) 545–557.
[43] G.A. Slack, J. Phys. Chem. Solid. 34 (1973) 321.
[44] S.L. Shinde, J. Goela, Condens. Matter Phys. XVIII 271 (2006) 133.
[45] M.A. Blanco, E. Francisco, V. Luāna, Comput. Phys. Commun. 158 (2004) 57. Source code distributed by the CPC program library: http://cpc.cs.qub.ac.uk/.
[46] C. Toher, et al., Phys. Rev. B 90 (2014), 174107.
[47] M. Blanco, et al., J. Mol. Struct. Theochem. 368 (1996) 245.
[48] J.-P. Poirier, Introduction to the Physics of the Earth's Interior, Cambridge University Press, 2000.
[49] J.-C. Zheng, Front. Phys. China 3 (2008) 269.
[50] B.R. Nag, Electron Transport in Compound Semiconductors, Springer, New York, 1980, pp. 171–229.
[51] T.J. Scheidemantel, et al., Phys. Rev. B 68 (2003), 125210.
[52] T. Thonhauser, et al., Phys. Rev. B 68 (2003), 085201.
[53] H. Kim, et al., Apl. Mater. 3 (4) (2015), 041506.
[54] M. Hammou, et al., Spin, World Scientific Publishing Company 10 (4) (2020, December), 2050029.
[55] B. Anissa, J. Mod. Phys. B 33 (22) (2019), 1950247.
[56] T. Ghellab, H. Baaziz, Z. Charifi, M. Telfah, A. Alsaad, A. Telfah, R. Hergenroder, R. Sabirianov, Mater. Sci. Semicond. Process. 141 (2022), 106415.
[57] H. Zhang, et al., J. Alloys Compd. 654 (2016) 321.
[58] K. Synoradzki, et al., Materials 12 (2019) 1723.
[59] T. Ghellab, H. Baaziz, Z. Charifi, K. Bouferrache, Ş. Uğur, G. Uğur, H. Ünver, Int. J. Mod. Phys. B 33 (2019), 1950234.
[60] T. Ghellab, H. Baaziz, Z. Charifi, K. Bouferrache, M.A. Saeed, A. Telfah, Mater. Res. Express 6 (2019), 075906.
[61] I. Mili, H. Latelli, T. Ghellab, Z. Charifi, H. Baaziz, F. Soyalp, Int. J. Mod. Phys. B 35 (7) (2021), 2150100.
[62] A. Telfah, T. Ghellab, H. Baaziz, Z. Charifi, A.M. Alsaad, R. Sabirianov, J. Magn. Magn Mater. 562 (2022), 169822.
[63] Z. Charifi, T. Ghellab, H. Baaziz, F. Soyalp, Int. J. Energy Res. (2022) 1-19.